

MAT: Multi-Range Attention Transformer for Efficient Image Super-Resolution

Chengxing Xie, Xiaoming Zhang, Linze Li, Yuqian Fu, Biao Gong, Tianrui Li, *Senior Member, IEEE*, Kai Zhang

Abstract—Image super-resolution (SR) has significantly advanced through the adoption of Transformer architectures. However, conventional techniques aimed at enlarging the self-attention window to capture broader contexts come with inherent drawbacks, especially the significantly increased computational demands. Moreover, the feature perception within a fixed-size window of existing models restricts the effective receptive field (ERF) and the intermediate feature diversity. We demonstrate that a flexible integration of attention across diverse spatial extents can yield significant performance enhancements. In line with this insight, we introduce Multi-Range Attention Transformer (MAT) for SR tasks. MAT leverages the computational advantages inherent in dilation operation, in conjunction with self-attention mechanism, to facilitate both multi-range attention (MA) and sparse multi-range attention (SMA), enabling efficient capture of both regional and sparse global features. Combined with local feature extraction, MAT adeptly capture dependencies across various spatial ranges, improving the diversity and efficacy of its feature representations. We also introduce the MSConvStar module, which augments the model’s ability for multi-range representation learning. Comprehensive experiments show that our MAT exhibits superior performance to existing state-of-the-art SR models with remarkable efficiency ($\sim 3.3\times$ faster than SRFormer-light). The codes are available at <https://github.com/stella-von/MAT>.

Index Terms—Transformer, image super-resolution, multi-range attention, efficient.

I. INTRODUCTION

Single image super-resolution (SISR) is a long-standing problem in the low-level vision community that aims to restore a high-resolution (HR) image from its low-resolution (LR) counterpart. It is an ill-posed inverse problem with an infinite number of solutions since one LR image can be theoretically degraded from infinite HR images. To be well-posed, it is essential to constrain the solution space by

Manuscript received December 18, 2024; revised February 6, 2025; accepted March 17, 2025. This work was supported by the Science Fund Program for Distinguished Young Scholars (Overseas), and Sichuan Province Science and Technology Support Program (Grand Nos. 2024NSFTD0036, 2024ZHC0166). This article was recommended by Associate Editor Dr. Zhijun Lei. (*Corresponding author: Kai Zhang.*)

Chengxing Xie, Xiaoming Zhang, Linze Li, Tianrui Li are with School of Computing and Artificial Intelligence, Southwest Jiaotong University, China. (email: {zxc0074869, zxiaoming360, linze.longyue}@gmail.com, trli@swjtu.edu.cn). Xiaoming Zhang is also with DAMO Academy, Alibaba Group, China.

Yuqian Fu is with INSAIT, Sofia University "St. Kliment Ohridski", Bulgaria. (e-mail: yuqian.fu@insait.ai).

Biao Gong is with Ant Group, China. (e-mail: a.biao.gong@gmail.com).

Kai Zhang is with the School of Intelligence Science and Technology, Nanjing University, China (e-mail: kaizhang@nju.edu.cn).

Chengxing Xie and Xiaoming Zhang contributed equally to this work.

Digital Object Identifier 10.1109/TCSVT.2025.3553135

Copyright ©2025 IEEE. Personal use of this material is permitted.

However, permission to use this material for any other purposes must be obtained from the IEEE by sending an email to pubs-permissions@ieee.org.

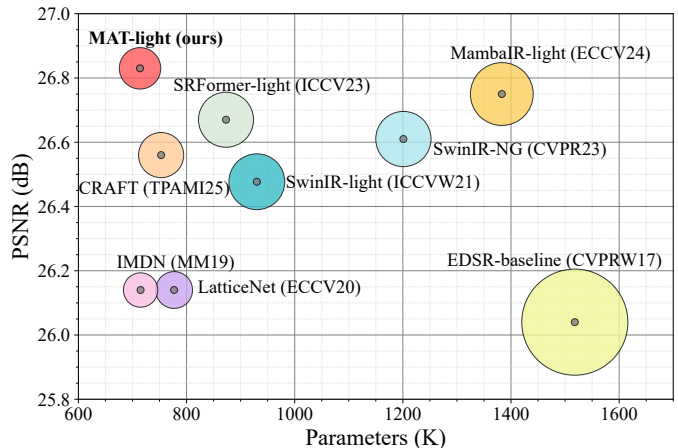


Fig. 1. Comparison of trade-offs between model performance and overheads on Urban100 [6] for $\times 4$ SR. The area of each circle denotes the Multi-Adds of these models. Our MAT-light achieves optimal SR performance with fewer parameters and Multi-Adds.

incorporating effective image priors. Two fundamental priors widely used for this purpose are image *locality* [1], [2] and *redundancy* [3]–[5]. The former indicates that image pixels exhibit strong correlations with their immediate neighbors while having weaker connections to distant pixels, while the latter suggests that similar patterns frequently recur at different locations within images¹, as shown in Fig. 2 (a). This manifests a conspicuous intuition that *both local and non-local dependencies are beneficial for SISR tasks, but not all global dependencies*. These priors suggest that while both local and non-local dependencies contribute to SISR tasks, not all global dependencies are equally valuable. For example, when reconstructing one eye in a human face, the pixels within the target region are highly correlated, and the non-local information from the other eye provides useful reference features, while smooth areas like skin and background offer less meaningful information.

In deep learning-based SISR methods, image locality is primarily preserved through convolutional operations, which extract local features within a fixed-size region (e.g., $k \times k$) using learnable kernels. This approach enables the regularization of the ill-posed inverse problem by learning locality priors from large-scale datasets. Various convolutional neural network (CNN) architectures have successfully implemented this principle, ranging from the pioneering SRCNN [7] to more designs including residual networks [8]–[10], dense connection

¹This phenomenon is also known as image self-similarity.

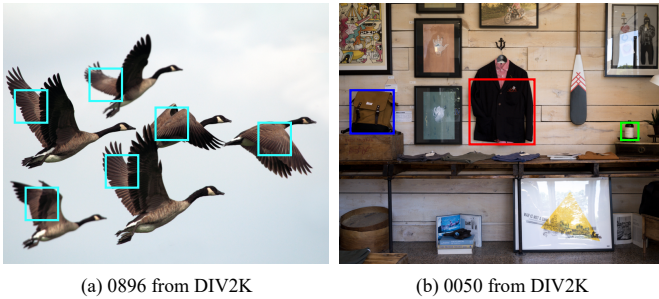


Fig. 2. (a) Illustration of image redundancy in natural images with self-similarity. Efficiently utilizing similar and repetitive structures and elements in natural images can aid in the reconstruction of image features. (b) In natural images, features can be observed to form a hierarchical structure across different spatial scales. The single and fixed-size WSA is insufficient to fully leverage such hierarchical features.

models [11], [12], information distillation networks [13]–[15], and attention-based approaches incorporating both channel [16] and spatial attention [17], [18]. CNN-based methods are inherently limited by their fixed-size convolutional kernels and local receptive fields, restricting their ability to capture broader contextual information and utilize global features effectively in HR image reconstruction.

Transformers [19] employ self-attention mechanisms that excel at capturing long-range dependencies and extracting features across extensive spatial regions, making them particularly effective for SR tasks [20]. Recent studies [21]–[23] have demonstrated the superiority of Transformer-based approaches over CNN-based methods in SR, particularly through enhanced window self-attention (WSA) mechanisms in Vision Transformers. However, expanding the window size to increase the effective receptive field (ERF) [24] leads to quadratic growth in computational complexity, creating significant efficiency challenges [23]. Furthermore, while natural images inherently contain hierarchical features at various spatial scales, as illustrated in Fig. 2 (b), most WSA-based models rely on homogeneous operators with fixed window sizes (e.g., 8×8 or 16×16). This limitation constrains their ability to effectively capture dependencies across different spatial ranges. Therefore, our primary goal is to develop an approach that enables efficient and flexible feature capture across multiple spatial ranges.

Building upon the principles of image *locality* and *redundancy*, we recognize that effectively processing features at different spatial ranges while **selectively** utilizing non-local information is crucial for SR tasks. To leverage this insight, we develop an approach that exploits hierarchical features at local, regional, and global levels to enhance the model’s multi-range representation learning capacity [25]. First, we construct a Local Aggregation Block (LAB) that combines convolution and channel attention [16] for efficient local feature aggregation. Inspired by the success of commonly-used dilated convolutions [26], [27], we incorporate dilation operations into the attention mechanism to expand the perceptual scope to both regional and global levels without increasing computational complexity.

We first replace standard convolution computation with an attention mechanism to achieve regional attention. Then, by

introducing holes in the attention region, similar to dilated convolutions, we implement efficient sparse global attention. To overcome the limitations of homogeneous operators in multi-scale feature capture, we extend these concepts into multi-range attention (MA) and sparse multi-range attention (SMA). Both MA and SMA operate across multiple regional ranges, achieving a larger effective receptive field than fixed-size attention windows. Additionally, we introduce the MSCConvStar module as a replacement for the traditional feed-forward network (FFN), enhancing image token interactions through the integration of multi-scale convolution (MSCConv) with star operation [28].

Based on the aforementioned designs, we present the Multi-Range Attention Transformer (MAT), a novel architecture for image SR that effectively captures features across diverse spatial ranges to enhance detail reconstruction. The lightweight variant, MAT-light, achieves state-of-the-art performance with remarkable efficiency when trained solely on the DIV2K [29] dataset, achieving state-of-the-art performance with lower computational complexity (e.g., **26.83dB**@Urban100 $\times 4$ with only **714K** parameters), as shown in Fig. 1. Similarly, in classical image SR tasks, MAT demonstrates superior performance while maintaining lower computational complexity. The key contributions of this work are:

- (1) We introduce MA and SMA, two complementary mechanisms that enable flexible capture of multi-range regional characteristics and sparse global attributes, advancing multi-range representation learning in SR tasks.
- (2) We develop the MSCConvStar module, an efficient alternative to conventional FFNs, designed specifically to enhance multi-range feature capture through the integration of hierarchical feature processing.
- (3) We propose **MAT**, a novel and computationally efficient SR architecture that consistently outperforms the current state of the art while requiring fewer computational resources, as validated through extensive experimentation.

II. RELATED WORKS

A. CNN-based Image SR

CNNs have dominated SR approaches since the introduction of SRCNN [7]. VDSR [8] employs a deeper network architecture, integrating residual learning to enhance performance metrics. EDSR [10] enhances the generalization ability of the model by removing the BatchNorm [30] layers, which were found to impede SR performance. RDN [11] implements dense connections for better hierarchical feature utilization, while RCAN [16] introduces channel attention to dynamically adjust feature importance. IGNN [31], NLSN [18], and FPAN [32] incorporate non-local attention [33] to capture global image characteristics. For resource-constrained applications, several approaches [13], [14] employ information distillation to create lightweight models. However, despite various enhancements including attention mechanisms [16], [18], large kernel convolutions [15], and partial channel shifting [2], CNN-based SR networks remain limited in their information perception range, struggling to model long-range dependencies [22].

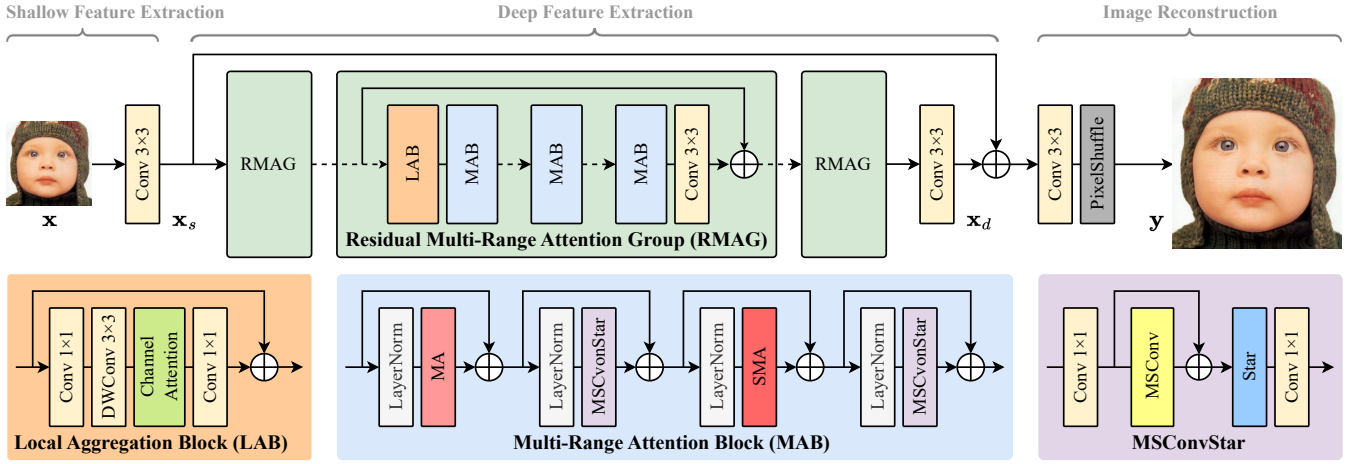


Fig. 3. The overall architecture of Multi-Range Attention Transformer (MAT).

B. Transformer-based Image SR

Vision Transformers have demonstrated remarkable success across diverse visual tasks [34]–[43]. Their superior ability to capture long-range dependencies and extract features from extensive regions makes them particularly effective for SR tasks. SwinIR [21] successfully adapts Swin-Transformer [35] architecture for image restoration, while Omni-SR [44] enhances performance by simultaneously modeling spatial and channel interactions. While ART [45] combines dense and sparse attention mechanisms to expand the receptive field, it suffers from implementation inefficiencies. HAT [22] and SRFormer [23] improve performance through enlarged self-attention windows. However, WSA-based methods face efficiency challenges as window size increases, resulting in quadratic computational growth and higher memory requirements. Additionally, fixed-size window partitioning limits flexible multi-scale information integration. Our work addresses these limitations by incorporating dilation operations into self-attention mechanisms, enabling flexible perception range expansion without additional computational overhead.

C. Hierarchical Feature Representation

Hierarchical feature representation has emerged as a fundamental component in diverse visual tasks [13], [25], [46]–[48]. Recent approaches have explored various strategies to leverage this concept: DMFN [46] achieves multi-scale feature perception through coordinated upsampling and downsampling operations, while Slide-Transformer [47] and DilateFormer [48] enhance the receptive field of 3×3 attention windows using deformed shifting and dilation operations, respectively. Although these methods demonstrate progress, their effective receptive fields remain limited, particularly when processing high-resolution images. While GRL [25] addresses this limitation by introducing anchored stripe self-attention and implementing a global-regional-local framework, its architectural complexity impedes practical deployment. In contrast, our approach achieves superior hierarchical feature representation while maintaining computational efficiency.

III. METHODOLOGY

A. Overall Architecture of MAT

Following established approaches [21], [22], our proposed MAT architecture, illustrated in Fig. 3, comprises three primary modules: shallow feature extraction, deep feature extraction, and image reconstruction. Given an LR input $\mathbf{x} \in \mathbb{R}^{H \times W \times 3}$, shallow features $\mathbf{x}_s \in \mathbb{R}^{H \times W \times C}$ are first extracted using a 3×3 convolutional layer:

$$\mathbf{x}_s = H_{SF}(\mathbf{x}), \quad (1)$$

where C denotes the channel dimension and $H_{SF}(\cdot)$ represents the convolution operation. The shallow features \mathbf{x}_s then is fed into the deep feature extraction through a series of residual multi-range attention groups (RMAG) followed by a 3×3 convolution, denoted as H_{DF} , to produce deep features $\mathbf{x}_d \in \mathbb{R}^{H \times W \times C}$:

$$\mathbf{x}_d = H_{DF}(\mathbf{x}_s). \quad (2)$$

Each RMAG integrates a local aggregation block (LAB), multiple multi-range attention blocks (MAB), a 3×3 convolution, and a residual connection, as depicted in Fig. 3. The shallow and deep features are combined to enhance convergence, followed by the reconstruction module H_{RC} (comprising convolution and PixelShuffle [49]) to generate the final HR image $\mathbf{y} \in \mathbb{R}^{H \times W \times 3}$:

$$\mathbf{y} = H_{RC}(\mathbf{x}_s + \mathbf{x}_d). \quad (3)$$

Notably, this architectural framework aligns with established approaches [16], [21], [23], [44], ensuring fair comparison with off-the-shelf methods. The model is optimized with \mathcal{L}_1 loss between the reconstructed image and the ground-truth HR image:

$$L(\theta) = \arg \min_{\theta} \frac{1}{N} \sum_{i=1}^N \|H_{MAT}(I_{LR}^i; \theta) - I_{HR}^i\|_1, \quad (4)$$

where $H_{MAT}(\cdot)$ denotes MAT model, θ denotes the learnable parameters, and N is the number of LR-HR training pairs.

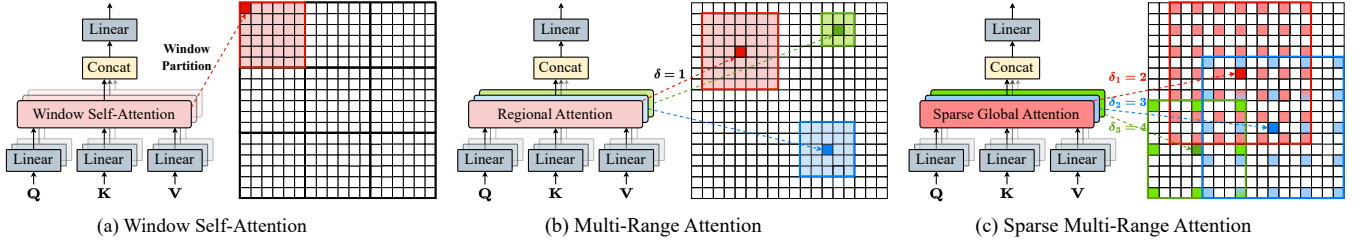


Fig. 4. Illustration of the window self-attention (WSA), multi-range attention (MA) and sparse multi-range attention (SMA). MA and SMA set different range sizes for different attention heads, enabling the multi-range representation learning.

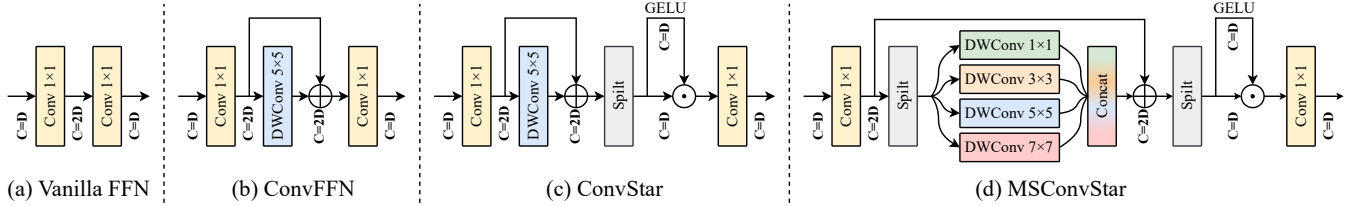


Fig. 5. Illustration of FFN [21], ConvFFN [23], ConvStar and MSCConvStar. \odot : element-wise multiplication (star).

B. Attention Mechanisms

Self-Attention. Self-attention (SA) [19] transforms input sequences through weighted aggregation of value vectors, where weights are determined by query-key interactions. Given a query \mathbf{Q} , and corresponding key-value pairs \mathbf{K} and \mathbf{V} , SA computes scaled dot-product attention, normalized through a softmax function, to generate attention weights for value aggregation. This process can be formally expressed as:

$$\text{SA}(\mathbf{Q}, \mathbf{K}, \mathbf{V}) = \text{Softmax}\left(\frac{\mathbf{Q}\mathbf{K}^T}{\sqrt{d}} + B\right) \mathbf{V}, \quad (5)$$

where d denotes the embedding dimension and B represents a learnable relative positional bias. While SA effectively captures global features and enhances texture details, its direct application to SR tasks presents two significant challenges: potential over-weighting of noise information and substantial computational overhead [18], [50].

Multi-Range Attention. While WSA has been widely adopted [34], [35] to balance computational efficiency and performance (Fig. 4 (a)), its effectiveness is limited by rigid window partitioning and computational constraints, which restrict flexible window sizing and broader spatial feature perception. To address these limitations, we propose restricting attention computation to specific neighborhoods, analogous to convolution operations, implementing a regional attention (RA) mechanism through sliding calculations. For RA with range size k , the key-value set for pixel $p_{i,j}$ at position (i, j) is confined to a $k \times k$ region, denoted as $\rho_{i,j}^k$. Given a feature map of dimensions $H \times W$, the RA computation for this pixel is expressed as:

$$\text{RA}_k(p_{i,j}) = \text{Softmax}\left(\frac{\mathbf{Q}_{i,j} \mathbf{K}_{\rho_{i,j}^k}^T}{\sqrt{d}} + B\right) \mathbf{V}_{\rho_{i,j}^k}, \quad (6)$$

where $1 \leq i \leq W$ and $1 \leq j \leq H$. Complete RA is achieved by applying this computation across all feature pixels. While various implementations of RA exist, including SASA [51], natten [52], and HaloNet [53], we adopt the efficient natten [52] approach. To overcome the limitations

of homogeneous operators in multi-scale feature capture, we extend RA to multi-range attention (MA) as shown in (Fig. 4 (b)):

$$\text{MA}(p_{i,j}) = H_F(\text{Concat}(\text{RA}_{k_1}, \dots, \text{RA}_{k_n})), \quad (7)$$

where k_1, \dots, k_n represent n different regional ranges, and H_F denotes the feature fusion module. By simultaneously processing information from multiple spatial ranges, MA effectively addresses the constraints of fixed-size window partitioning in WSA.

Sparse Multi-Range Attention. MA can be generalized to sparse multi-range attention (SMA), akin to dilated convolutions, as shown in Fig 4. Dilating the region prompts the model to capture an extended array of associations for the target pixel. We expand RA through dilation operation to achieve sparse global attention (SGA). Specifically, for SGA with a range size of k and a dilation rate of δ , the key-value set corresponding to the (i, j) -th pixel $p_{i,j}$ is limited to a sparse neighborhood of size $k_d \times k_d$, denoted as $\rho_{i,j}^{k,\delta}$, where $k_d = k + (k-1) \cdot (\delta-1)$. The SGA of the pixel $p_{i,j}$ can be defined as:

$$\text{SGA}_k^\delta(p_{i,j}) = \text{Softmax}\left(\frac{\mathbf{Q}_{i,j} \mathbf{K}_{\rho_{i,j}^{k,\delta}}^T}{\sqrt{d}} + B\right) \mathbf{V}_{\rho_{i,j}^{k,\delta}}. \quad (8)$$

The keys and values corresponding to the (i, j) -th pixel $p_{i,j}$ will be selected from the following set (i', j') for self-attention computation:

$$\left\{ (i', j') \mid i' = i + x \times \delta, j' = j + y \times \delta \right\}, \quad (9)$$

where $-\frac{k}{2} \leq x, y \leq \frac{k}{2}$. Subsequently, by aggregating SGAs from multiple ranges, we achieve SMA:

$$\text{SMA}(p_{i,j}) = H_F\left(\text{Concat}\left(\text{SGA}_{k_1}^{\delta_1}, \dots, \text{SGA}_{k_n}^{\delta_n}\right)\right), \quad (10)$$

where $\delta_1, \dots, \delta_n$ represent n types of dilation rates. The sparse area size can be flexibly enlarge by adjusting dilation rates, all while without introducing computational overhead.

C. Multi-Range Representation Learning

MSConvStar. The conventional feed-forward network (FFN) in Transformer architectures [19] utilizes two linear projections with an activation function, essentially implementing a basic multi-layer perceptron (MLP) for image token interaction. However, this structure proves inadequate for modeling complex, hierarchical spatial relationships, limiting SR model performance. While recent approaches [23], [38] incorporate convolutions into MLPs to enhance spatial feature learning, they operate at a single scale. To address these limitations, we propose the multi-scale convolution star (MSConvStar) module, which enhances token representation through the integration of multi-scale convolution (MSConv) and star operations [28], as illustrated in Fig. 5. This module combines parallel depth-wise convolutions at different scales with residual connections, working synergistically with multi-range attention to enhance spatial relationships. The star operation also enables nonlinear feature space transformation without increasing network width, thereby improving the model’s expressive capacity.

Multi-Range Dependencies. Most SR models [10], [21], [23], [54] typically overlook the inherent hierarchical features in natural images, relying instead on homogeneous operators for structural modeling. Our MAT addresses this limitation by explicitly modeling three distinct types of dependencies across different spatial scales through specialized components: LAB, MA, and SMA (Fig. 3). LAB captures local neighborhood dependencies through depth-wise convolutions and channel attention [16], while MA and SMA model regional attributes and sparse global information, respectively. Recognizing that long-range dependencies are relatively weaker, we incorporate MA and SMA within a Transformer framework [19], replacing the traditional MLP with our MSConvStar to create the MAB module for enhanced feature learning. This comprehensive approach enables more effective spatial structure modeling, enriches intermediate feature diversity, and ultimately yields more precise detail reconstruction.

IV. EXPERIMENTS

A. Experimental Settings

Datasets and Evaluation. Follow previous works [21], [23], we train two versions of MAT: lightweight and classical. For lightweight image SR, we utilize DIV2K [29] dataset to train our MAT-light. For classical version, the DF2K (DIV2K [29] + Flickr2K [10]) is employed. Our evaluation of the models is performed on five commonly used benchmark datasets, including Set5 [55], Set14 [56], B100 [57], Urban100 [6], and Manga109 [58]. The PSNR (dB) and SSIM scores, calculated on the luminance (Y) channel, are used to evaluate the performance of the model.

Implementation Details. For the lightweight image SR, we set the number of RMAG, MAB and channel to 4, 2, and 60, respectively. The range sizes of MA and SMA are both set to 7×7 , 9×9 , and 11×11 . The dilation rates of SMA are set to the floor division of the input patch size (64×64) by the range sizes, i.e., 9, 7, and 5. The total number of attention heads is set to 6, with two heads allocated to each range size. For

TABLE I
ABLATION STUDY ON EACH COMPONENT.

MD	MSConvStar	MR	Params. (K)	Multi-Adds (G)	Urban100 PSNR (dB) / SSIM
✗	✗	✗	670	185.2	32.59 / 0.9329
✓	✗	✗	709	192.4	32.93 / 0.9357
✓	✓	✗	693	188.4	33.11 / 0.9374
✓	✓	✓	694	189.6	33.22 / 0.9381

the classical image SR, the the number of RMAG, MAB and channel increase to 6, 3, and 156, respectively. The range sizes increase to 13×13 , 15×15 and 17×17 . The training patch size is set to 64×64 . For data augmentation, we randomly rotate and horizontally flip the input patches. We employ Adam [59] optimizer with $\beta_1 = 0.9$ and $\beta_2 = 0.99$ to train the model, with a total of 500k iterations. The initial learning rate is set at 2×10^{-4} and is halved at [250k, 400k, 450k, 475k].

B. Ablation Study

We conduct comprehensive ablation experiments using lightweight SR models trained from scratch on DIV2K ($\times 2$) and evaluated on Urban100 for $\times 2$ SR. To ensure fair comparison, all models maintain consistent training protocols and hyperparameters. Additionally, we provide the Multi-Adds metric for each model, which is computed based on upscaling a single image input to a resolution of 1280×720 .

Effectiveness of Each Component. We systematically evaluate the contribution of each proposed component through detailed ablation experiments, as presented in Table I. **Firstly, baseline configuration.** Our baseline model adapts SwinIR-light by replacing its Transformer blocks with regional attention (9×9 range size, comparable to SwinIR-light’s window size) and reducing the number of Transformer blocks to four per layer. **Secondly, multi-range dependencies (MD).** Integration of LAB and sparse global attention enables feature capture across diverse spatial ranges, significantly enhancing model performance. **Thirdly, MSConvStar integration.** Replacing the conventional MLP with MSConvStar improves feature representation capability while reducing both parameter count and computational overhead. **Finally, multi-range (MR) strategy.** Extending single-region attention to multi-range attention expands the model’s receptive field, yielding our final MAT-light architecture, improved performance with minimal computational cost increase. These sequential improvements demonstrate the effectiveness of each component, as further validated through reverse-order ablation experiments.

Effects of Dilation Rate. The dilation strategy in MAT enables broader information capture, enhancing overall performance. We investigate the optimal dilation rate δ through systematic experimentation, with results presented in Table II. Here, $\delta = 1$ represents standard MA, while $\delta = \text{Maximum}$ indicates SMA with dilation rate set to the floor division of the input feature map size by the range size. Our experiments reveal a positive correlation between performance and dilation rate, with optimal results achieved at $\delta = \text{Maximum}$. However, further increasing the dilation rate through padding leads to significant performance degradation, likely due to the introduction of irrelevant elements that compromise attention

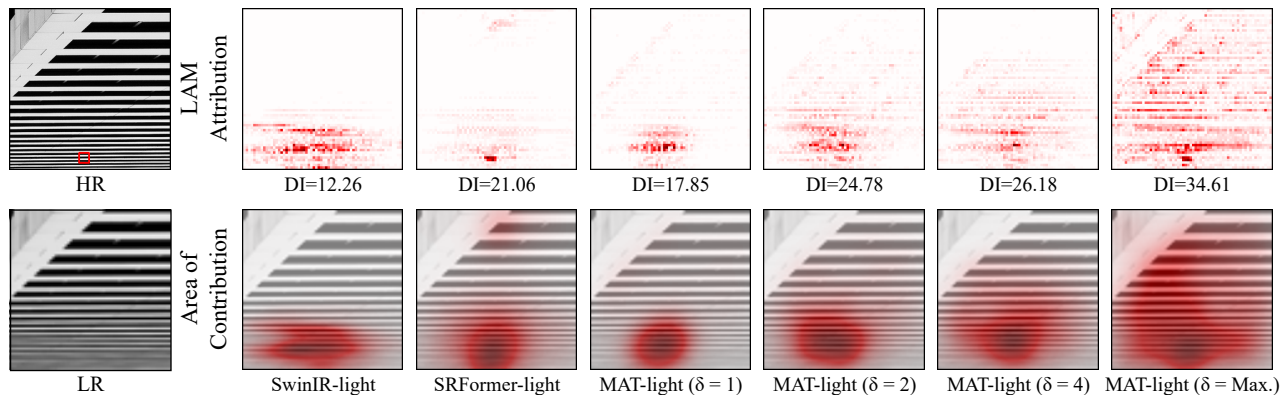


Fig. 6. LAM [20] results of SwinIR [21], SRFormer [23] and our MAT with various dilation rates. The experiments is conducted using lightweight models. The LAM attribution indicates the importance of each pixel in LR input with respect to the SR result of the patch marked with a red box. The diffusion index (DI) [20] reflects the range of involved pixels, and a higher DI indicates a broader range of pixels available to the model. δ denotes the dilation rate of MAT-light. The results indicate that, SRFormer-light, due to the use of larger windows (i.e. 16×16), can leverage more information compared to SwinIR-light. Additionally, MAT-light can use the most pixels for reconstruction by increasing the dilation rate without introducing additional computational burden.

TABLE II

EFFECTS OF DILATION RATE δ . NOTE $\delta = \text{MAXIMUM}$ INDICATES THAT THE DILATION RATE FOR SMA IS SET TO THE FLOOR DIVISION OF THE INPUT FEATURE MAP SIZE (64×64) BY THE RANGE SIZES (7, 9, 11).

Dilation Rate { $\delta_1, \delta_2, \delta_3$ }	{1, 1, 1}	{2, 2, 2}	{4, 4, 4}	{5, 7, 9} (Maximum)	{6, 8, 10} (Exceeding)
PSNR (dB)	32.94	33.11	33.16	33.22	29.60
SSIM	0.9358	0.9373	0.9378	0.9381	0.8743

TABLE III

ABLATION STUDY ON ATTENTION MECHANISMS.

Attention Type	Params. (K)	Multi-Adds (G)	Urban100	
			PSNR (dB)	SSIM
WA + SWA	687	179.2	32.89 / 0.9348	
DA + SA	667	>280	32.99 / 0.9358	
RA + SGA	693	188.4	33.11 / 0.9374	
MA + SMA	694	189.6	33.22 / 0.9381	

weight learning. Visual analysis using LAM [20] (Fig. 6) demonstrates that larger dilation rates expand the model’s perceptive field. Notably, MAT-light’s LAM attribution spans nearly the entire image, while competing models exhibit more restricted ranges of influence.

Effectiveness of Multi-Range Attention. We evaluate our multi-range attention (MA) mechanism against representative attention mechanisms: window attention (WA) [21], sparse attention (SA) [45], and regional attention (RA). As demonstrated in Table III and Fig. 7, ART’s combination of dense attention (DA) and sparse attention (SA) outperforms SwinIR’s window attention (WA) and shifted window attention (SWA), validating the effectiveness of sparse operations. However, ART’s [45] window partition-based sparse operation implementation limits token interval flexibility and incurs substantial computational overhead. Regional attention (RA) and sparse global attention (SGA) address these window partitioning limitations in DA and SA, yielding improved model performance. The extension to MA and SMA further enhances this improvement, achieving optimal performance metrics.

To further validate our approach, we visualize pre-upsampling feature maps across models with different attention strategies (Fig. 8). MAT-light demonstrates superior texture preservation and detail retention in feature represen-

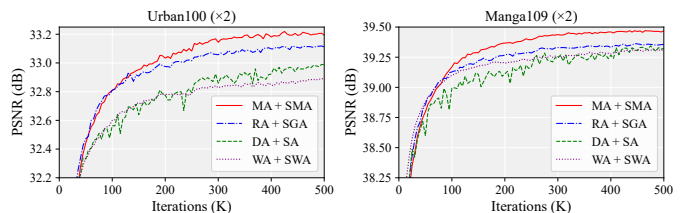


Fig. 7. PSNR (dB) comparison of different attention mechanisms on Urban100 and Manga109 datasets.

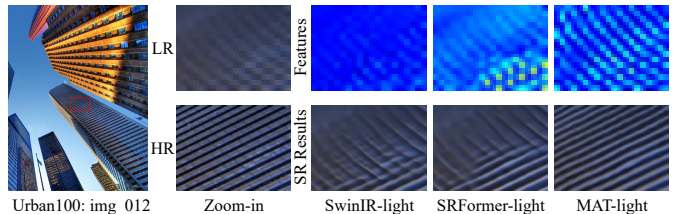


Fig. 8. Visual comparison of features and reconstruction results on $\times 4$ SR. MAT-light captures **holistic** structural patterns more effectively, highlighting its retention of crucial image details.

tations compared to alternative models, leading to sharper reconstruction results. These visualizations provide additional evidence that multi-range attention significantly enhances feature representation capabilities.

Effectiveness of MSConvStar. We evaluate MSConvStar through comparative analysis of four distinct configurations illustrated in Fig. 5. Results in Table IV demonstrate that integrating depth-wise convolutions into MLP enhances performance, underscoring the significance of spatial information modeling. The star operation further improves performance while reducing model complexity through enhanced non-linear expression. Our MSConvStar extends this framework to multi-scale convolutions, enabling richer feature capture across varied scales.

Effectiveness of Multi-Range Dependencies. MAT integrates multi-range features through three specialized components: local convolutions for local features, MA for regional features, and SMA for sparse global features. We evaluate four different feature integration schemes (Table V), maintaining consistent model parameters by adjusting MSConvStar’s 1×1 convolution channels. Experimental results demonstrate that omitting any feature hierarchy level degrades model performance, with

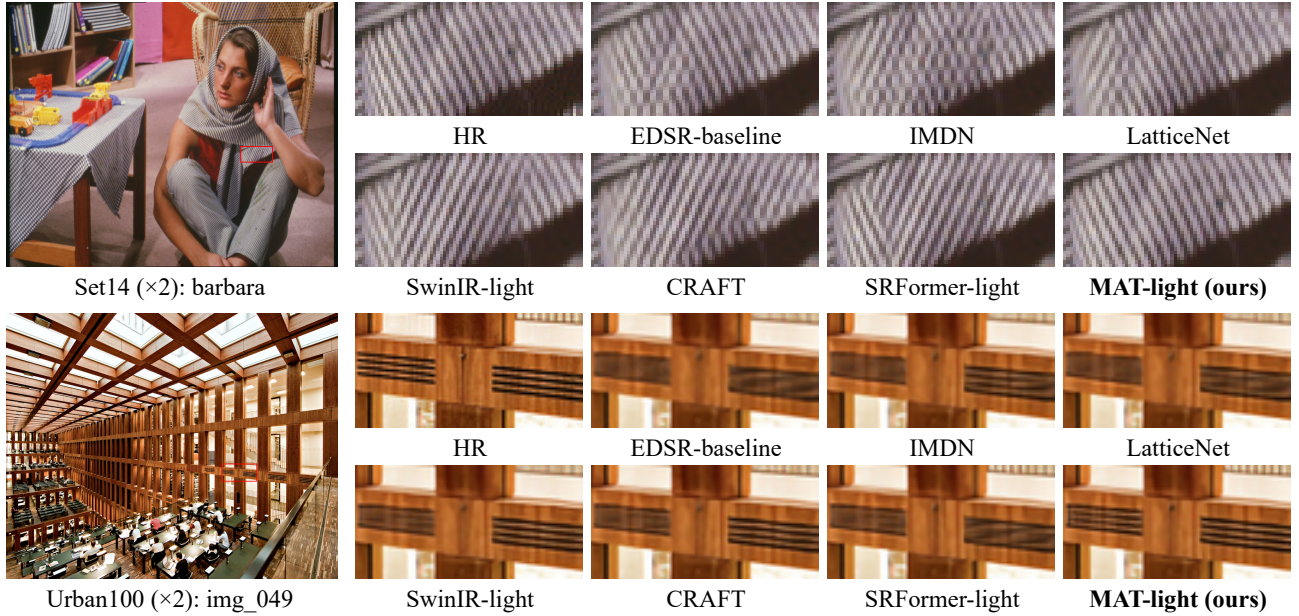


Fig. 9. Visual comparison on $\times 2$ **lightweight image SR**. The patches for comparison are marked with red boxes in the original images.

TABLE IV
ABLATION STUDY ON MSConvSTAR. THE SCHEMATIC DIAGRAM OF FOUR NETWORK STRUCTURAL COMBINATIONS IS SHOWN IN FIG. 5

Conv	Star	Multi-Scale	Params. (K)	Multi-Adds (G)	Urban100 PSNR (dB) / SSIM
✗	✗	✗	710	193.6	32.98 / 0.9359
✓	✗	✗	760	204.7	33.06 / 0.9367
✓	✓	✗	702	191.4	33.19 / 0.9379
✓	✓	✓	694	189.6	33.22 / 0.9381

TABLE V
ABLATION STUDY ON THE MULTI-RANGE DEPENDENCIES. WE ENSURE CONSISTENCY IN MODEL PARAMETERS BY ADJUSTING THE NUMBER OF CHANNELS IN THE 1×1 CONVOLUTION OF MSConvSTAR.

Local	Regional	Sparse	Global	Multi-Adds (G)	Urban100 PSNR (dB) / SSIM
✓	✓	✗	✗	189.6	32.94 / 0.9358
✓	✗	✓	✗	189.6	33.00 / 0.9366
✗	✓	✓	✗	189.7	33.15 / 0.9376
✓	✓	✓	✓	189.6	33.22 / 0.9381

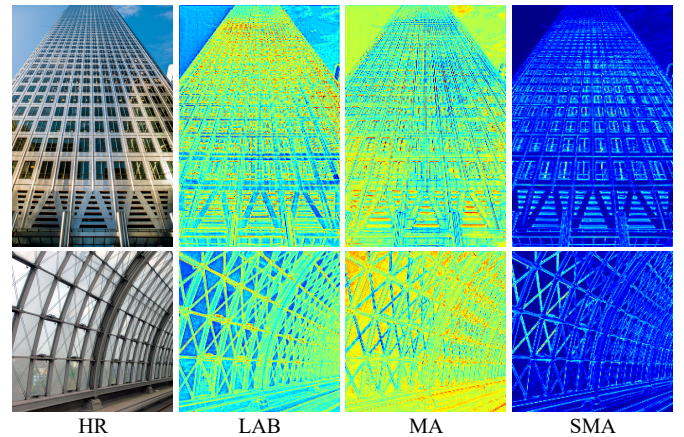


Fig. 11. Visualization of feature maps for multi-range dependencies. LAB and MA emphasize more on low-frequency structural information, while SMA focuses more on high-frequency edge details.

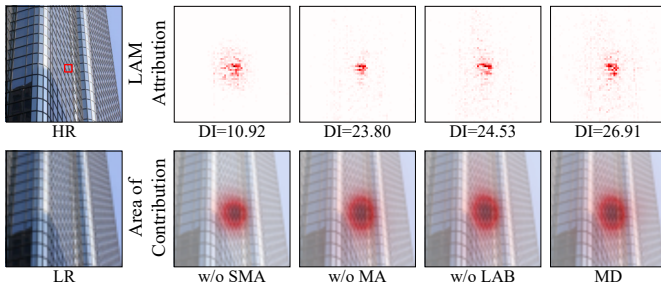


Fig. 10. LAM [20] results under different range dependency configurations.

larger-range features showing particularly significant impact.

We further analyze component contributions through LAM visualization across four model configurations (Fig. 10). Results indicate that removing any feature extraction mechanism diminishes model perceptual capabilities, with SMA removal causing the most significant reduction in perception range,

while MA or LAB removal yields more modest decrements. This pattern suggests SMA's primary role in non-local information processing, contrasting with LAB and MA's focus on local feature extraction. Feature map analysis (Fig. 11) reveals complementary roles: LAB and MA mainly capture low-frequency structural information, while SMA specializes in high-frequency edge details, enabling MAT to effectively model multi-range dependencies through synergistic feature extraction.

C. Lightweight Image Super-Resolution

To demonstrate the effectiveness and efficiency of proposed MAT, we compare our MAT-light with various recent state-of-the-art lightweight SR methods, including the EDSR-baseline [10], IMDN [13], LatticeNet [60], SwinIR-light [21], SwinIR-NG [61], Omni-SR [44], SRFormer-light [23], MambaIR-light [62], SRConvNet-L [63] and CRAFT [54].

TABLE VI

QUANTITATIVE COMPARISON (PSNR (dB) / SSIM) WITH STATE-OF-THE-ART METHODS FOR **LIGHTWEIGHT SR** ON FIVE BENCHMARK DATASETS. 'MULTI-ADDS' IS CALCULATED UNDER THE SETTING OF UPSCALING ONE IMAGE TO 1280×720 RESOLUTION. FOR A FAIR COMPARISON, **ONLY THE DIV2K DATASET IS USED FOR TRAINING**. THE BEST AND SECOND BEST RESULTS ARE MARKED WITH BOLD AND UNDERLINE, RESPECTIVELY. 'N/A' MEANS THAT THE RESULT IS NOT AVAILABLE.

Scale	Method	Annual	Params. (K)	Multi-Adds (G)	Set5 PSNR / SSIM	Set14 PSNR / SSIM	B100 PSNR / SSIM	Urban100 PSNR / SSIM	Manga109 PSNR / SSIM
×2	EDSR-baseline [10]	CVPRW17	1370	316.3	37.99 / 0.9604	33.57 / 0.9175	32.16 / 0.8994	31.98 / 0.9272	38.54 / 0.9769
	IMDN [13]	MM19	694	158.8	38.00 / 0.9605	33.63 / 0.9177	32.19 / 0.8996	32.17 / 0.9283	38.88 / 0.9774
	LatticeNet [60]	ECCV20	756	169.5	38.06 / 0.9607	33.70 / 0.9187	32.20 / 0.8999	32.25 / 0.9288	N/A
	SwinIR-light [21]	ICCVW21	910	252.9	38.14 / 0.9611	33.86 / 0.9206	32.31 / 0.9012	32.76 / 0.9340	39.12 / 0.9783
	SwinIR-NG [61]	CVPR23	1181	274.1	38.17 / 0.9612	33.94 / 0.9205	32.31 / 0.9013	32.78 / 0.9340	39.20 / 0.9781
	Omni-SR [44]	CVPR23	798	N/A	38.22 / 0.9613	33.98 / 0.9210	<u>32.36 / 0.9020</u>	<u>33.05 / 0.9363</u>	39.28 / 0.9784
	SRFormer-light [23]	ICCV23	853	236.2	<u>38.23 / 0.9613</u>	33.94 / 0.9209	<u>32.36 / 0.9019</u>	32.91 / 0.9353	39.28 / 0.9785
	MambaIR-light [62]	ECCV24	1363	278.9	38.16 / 0.9610	<u>34.00 / 0.9212</u>	32.34 / 0.9017	32.92 / 0.9356	39.31 / 0.9779
	SRConvNet-L [63]	IJCV25	885	160	38.14 / 0.9610	33.81 / 0.9199	32.28 / 0.9010	32.59 / 0.9321	39.22 / 0.9779
	CRAFT [54]	ICCV23&PAMI25	738	197.2	<u>38.23 / 0.9615</u>	33.92 / 0.9211	32.33 / 0.9016	32.86 / 0.9343	<u>39.39 / 0.9786</u>
	MAT-light	Ours	694	189.6	<u>38.28 / 0.9617</u>	<u>34.11 / 0.9227</u>	<u>32.41 / 0.9029</u>	<u>33.22 / 0.9381</u>	<u>39.46 / 0.9789</u>
×3	EDSR-baseline [10]	CVPRW17	1555	160.2	34.37 / 0.9270	30.28 / 0.8417	29.09 / 0.8052	28.15 / 0.8527	33.45 / 0.9439
	IMDN [13]	MM19	703	71.5	34.36 / 0.9270	30.32 / 0.8417	29.09 / 0.8046	28.17 / 0.8519	33.61 / 0.9445
	LatticeNet [60]	ECCV20	765	76.3	34.40 / 0.9272	30.32 / 0.8416	29.10 / 0.8049	28.19 / 0.8513	N/A
	SwinIR-light [21]	ICCVW21	918	114.5	34.62 / 0.9289	30.54 / 0.8463	29.20 / 0.8082	28.66 / 0.8624	33.98 / 0.9478
	SwinIR-NG [61]	CVPR23	1190	114.1	34.64 / 0.9293	30.58 / 0.8471	29.24 / 0.8090	28.75 / 0.8639	34.22 / 0.9488
	Omni-SR [44]	CVPR23	807	N/A	34.70 / 0.9294	30.57 / 0.8469	29.28 / 0.8094	28.84 / 0.8656	34.22 / 0.9487
	SRFormer-light [23]	ICCV23	861	104.8	34.67 / <u>0.9296</u>	30.57 / 0.8469	29.26 / 0.8099	28.81 / 0.8655	34.19 / 0.9489
	MambaIR-light [62]	ECCV24	1371	124.6	<u>34.72 / 0.9296</u>	<u>30.63 / 0.8475</u>	<u>29.29 / 0.8099</u>	<u>29.00 / 0.8689</u>	<u>34.39 / 0.9495</u>
	SRConvNet-L [63]	IJCV25	906	74	34.59 / 0.9288	30.50 / 0.8455	29.22 / 0.8081	28.56 / 0.8600	34.17 / 0.9479
	CRAFT [54]	ICCV23&PAMI25	744	87.5	34.71 / 0.9295	30.61 / 0.8469	29.24 / 0.8093	28.77 / 0.8635	34.29 / 0.9491
	MAT-light	Ours	703	85.0	<u>34.79 / 0.9303</u>	<u>30.68 / 0.8491</u>	<u>29.32 / 0.8116</u>	<u>29.03 / 0.8698</u>	<u>34.49 / 0.9505</u>
×4	EDSR-baseline [10]	CVPRW17	1518	114.0	32.09 / 0.8938	28.58 / 0.7813	27.57 / 0.7357	26.04 / 0.7849	30.35 / 0.9067
	IMDN [13]	MM19	715	40.9	32.21 / 0.8948	28.58 / 0.7811	27.56 / 0.7353	26.04 / 0.7838	30.45 / 0.9075
	LatticeNet [60]	ECCV20	777	43.6	32.18 / 0.8943	28.61 / 0.7812	27.57 / 0.7355	26.14 / 0.7844	N/A
	SwinIR-light [21]	ICCVW21	930	65.2	32.44 / 0.8976	28.77 / 0.7858	27.69 / 0.7406	26.47 / 0.7980	30.92 / 0.9151
	SwinIR-NG [61]	CVPR23	1201	63.0	32.44 / 0.8980	28.83 / 0.7870	27.73 / 0.7418	26.61 / 0.8010	31.09 / 0.9161
	Omni-SR [44]	CVPR23	819	N/A	32.49 / 0.8988	28.78 / 0.7859	27.71 / 0.7415	26.64 / 0.8018	31.02 / 0.9151
	SRFormer-light [23]	ICCV23	873	62.8	32.51 / 0.8988	28.82 / 0.7872	27.73 / 0.7422	26.67 / 0.8032	31.17 / 0.9165
	MambaIR-light [62]	ECCV24	1383	70.8	32.51 / <u>0.8993</u>	<u>28.85 / 0.7876</u>	<u>27.75 / 0.7423</u>	<u>26.75 / 0.8051</u>	<u>31.26 / 0.9175</u>
	SRConvNet-L [63]	IJCV25	902	45	32.44 / 0.8976	28.77 / 0.7857	27.69 / 0.7402	26.47 / 0.7970	30.96 / 0.9139
	CRAFT [54]	ICCV23&PAMI25	753	52.4	<u>32.52 / 0.8989</u>	<u>28.85 / 0.7872</u>	<u>27.72 / 0.7418</u>	26.56 / 0.7995	31.18 / 0.9168
	MAT-light	Ours	714	48.5	<u>32.61 / 0.8998</u>	<u>28.92 / 0.7897</u>	<u>27.79 / 0.7444</u>	<u>26.83 / 0.8088</u>	<u>31.38 / 0.9192</u>

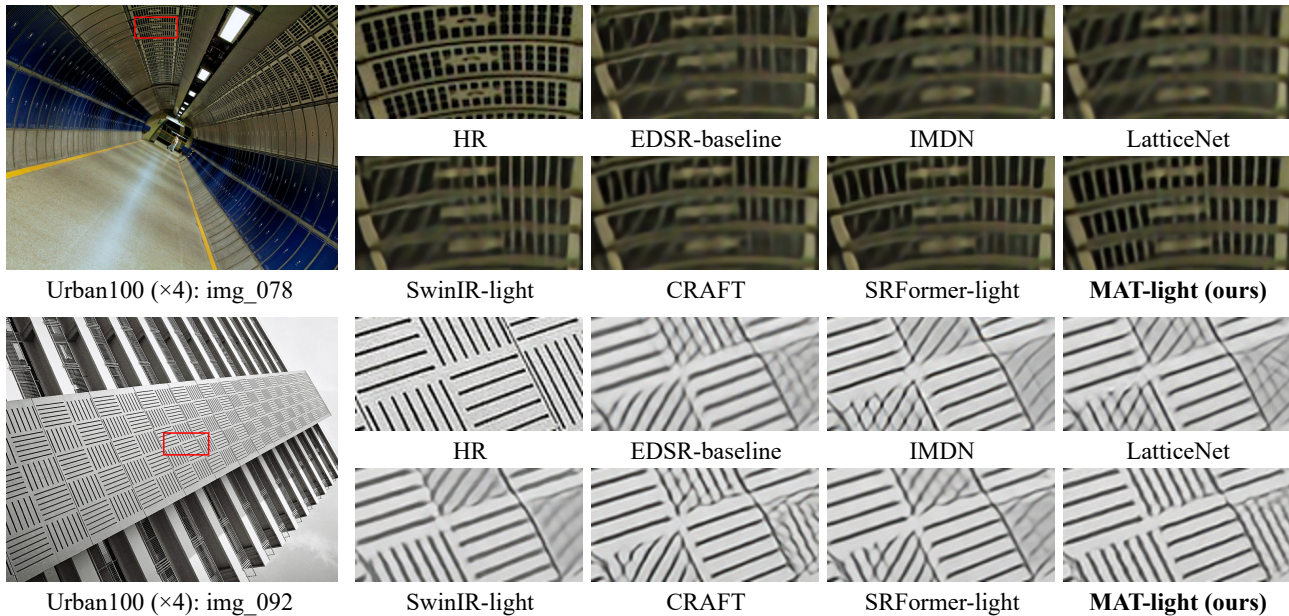


Fig. 12. Visual comparison on $\times 4$ **lightweight image SR**. The patches for comparison are marked with red boxes in the original images.

Quantitative Comparison. Table VI presents a quantitative comparison of lightweight image SR models. We report both model parameters and Multi-Adds to measure computational efficiency and complexity. Our MAT-light demonstrates the

best performance across all five benchmark datasets for various scale factors while maintaining the lowest parameter count and competitive computational complexity. Notably, compared to CNN-based approaches, MAT-light achieves substantial im-

TABLE VII

QUANTITATIVE COMPARISON (PSNR (dB) / SSIM) WITH STATE-OF-THE-ART METHODS FOR CLASSICAL SR ON FIVE BENCHMARK DATASETS. 'MULTI-ADDS' IS CALCULATED UNDER THE SETTING OF UPSCALING ONE IMAGE TO 256² RESOLUTION. THE BEST AND SECOND BEST RESULTS ARE MARKED IN BOLD AND UNDERLINE, RESPECTIVELY. 'N/A' MEANS THAT THE RESULT IS NOT AVAILABLE.

Scale	Method	Annual	Params. (M)	Multi-Adds (G)	Set5 PSNR / SSIM	Set14 PSNR / SSIM	B100 PSNR / SSIM	Urban100 PSNR / SSIM	Manga109 PSNR / SSIM
×2	EDSR [10]	CVPRW17	40.73	667.4	38.11 / 0.9602	33.92 / 0.9195	32.32 / 0.9013	32.93 / 0.9351	39.10 / 0.9773
	RCAN [16]	ECCV18	15.44	251.0	38.27 / 0.9614	34.12 / 0.9216	32.41 / 0.9027	33.34 / 0.9384	39.44 / 0.9786
	IGNN [31]	NeurIPS20	49.51	N/A	38.24 / 0.9613	34.07 / 0.9217	32.41 / 0.9025	33.23 / 0.9383	39.35 / 0.9786
	NLSN [18]	CVPR21	41.80	731.4	38.34 / 0.9618	34.08 / 0.9231	32.43 / 0.9027	33.42 / 0.9394	39.59 / 0.9789
	SwinIR [21]	ICCV21	11.75	205.3	38.42 / 0.9623	34.46 / 0.9250	32.53 / 0.9041	33.81 / 0.9427	39.92 / 0.9797
	ART-S [45]	ICLR23	11.71	227.6	38.48 / 0.9625	34.50 / 0.9258	32.53 / 0.9043	34.02 / 0.9437	40.11 / 0.9804
	HAT-S [22]	CVPR23	9.47	209.6	38.58 / 0.9628	34.70 / 0.9261	32.59 / 0.9050	<u>34.31</u> / 0.9459	40.14 / 0.9805
	DAT-S [64]	ICCV23	11.06	193.3	38.54 / 0.9627	34.60 / 0.9258	32.57 / 0.9047	34.12 / 0.9444	40.17 / 0.9804
	SRFormer [23]	ICCV23	10.38	206.4	38.51 / 0.9627	34.44 / 0.9253	32.57 / 0.9046	34.09 / 0.9449	40.07 / 0.9802
	FDRNet [65]	TIP24	8.66	N/A	38.54 / 0.9627	<u>34.65</u> / <u>0.9262</u>	32.57 / 0.9046	34.18 / 0.9449	40.10 / 0.9803
	MambaIR [62]	ECCV24	20.42	318.8	38.57 / 0.9627	<u>34.67</u> / <u>0.9261</u>	32.58 / 0.9048	34.15 / 0.9446	<u>40.28</u> / 0.9806
	MAT	Ours	9.60	187.0	<u>38.61</u> / <u>0.9631</u>	34.53 / 0.9259	<u>32.62</u> / <u>0.9053</u>	<u>34.31</u> / <u>0.9462</u>	40.22 / 0.9808
	MAT+	Ours	9.60	187.0	38.65 / 0.9632	34.60 / 0.9263	32.65 / 0.9056	34.44 / 0.9468	40.33 / 0.9811
×3	EDSR [10]	CVPRW17	43.68	315.9	34.65 / 0.9280	30.52 / 0.8462	29.25 / 0.8093	28.80 / 0.8653	34.17 / 0.9476
	RCAN [16]	ECCV18	15.63	112.1	34.74 / 0.9299	30.65 / 0.8482	29.32 / 0.8111	29.09 / 0.8702	34.44 / 0.9499
	IGNN [31]	NeurIPS20	49.51	N/A	34.72 / 0.9298	30.66 / 0.8484	29.31 / 0.8105	29.03 / 0.8696	34.39 / 0.9496
	NLSN [18]	CVPR21	44.75	344.1	34.85 / 0.9306	30.70 / 0.8485	29.34 / 0.8117	29.25 / 0.8726	34.57 / 0.9508
	SwinIR [21]	ICCV21	11.94	98.5	34.97 / 0.9318	30.93 / 0.8534	29.46 / 0.8145	29.75 / 0.8826	35.12 / 0.9537
	ART-S [45]	ICLR23	11.90	102.0	34.98 / 0.9318	30.94 / 0.8530	29.45 / 0.8146	29.86 / 0.8830	35.22 / 0.9539
	HAT-S [22]	CVPR23	9.66	119.7	35.01 / 0.9325	<u>31.05</u> / <u>0.8550</u>	29.50 / 0.8158	<u>30.15</u> / <u>0.8879</u>	35.40 / 0.9547
	DAT-S [64]	ICCV23	11.25	88.3	<u>35.12</u> / 0.9327	31.04 / 0.8543	29.51 / 0.8157	<u>29.98</u> / <u>0.8846</u>	35.41 / 0.9546
	SRFormer [23]	ICCV23	10.56	93.2	35.02 / 0.9323	30.94 / 0.8540	29.48 / 0.8156	30.04 / 0.8865	35.26 / 0.9543
	FDRNet [65]	TIP24	8.85	N/A	34.98 / 0.9320	30.98 / 0.8535	29.47 / 0.8152	29.97 / 0.8856	35.24 / 0.9540
	MambaIR [62]	ECCV24	20.61	142.0	35.08 / 0.9323	30.99 / 0.8536	29.51 / 0.8157	29.93 / 0.8841	<u>35.43</u> / 0.9546
	MAT	Ours	9.78	83.9	35.09 / 0.9328	31.03 / 0.8550	<u>29.53</u> / <u>0.8167</u>	30.11 / 0.8879	35.41 / 0.9549
	MAT+	Ours	9.78	83.9	35.13 / 0.9330	31.08 / 0.8555	29.56 / 0.8171	30.22 / 0.8893	35.55 / 0.9554
×4	EDSR [10]	CVPRW17	43.09	205.8	32.46 / 0.8968	28.80 / 0.7876	27.71 / 0.7420	26.64 / 0.8033	31.02 / 0.9148
	RCAN [16]	ECCV18	15.59	65.3	32.63 / 0.9002	28.87 / 0.7889	27.77 / 0.7436	26.82 / 0.8087	31.22 / 0.9173
	IGNN [31]	NeurIPS20	49.51	N/A	32.57 / 0.8998	28.85 / 0.7891	27.77 / 0.7434	26.84 / 0.8090	31.28 / 0.9182
	NLSN [18]	CVPR21	44.16	221.8	32.59 / 0.9000	28.87 / 0.7891	27.78 / 0.7444	26.96 / 0.8109	31.27 / 0.9184
	SwinIR [21]	ICCV21	11.90	53.8	32.92 / 0.9044	29.09 / 0.7950	27.92 / 0.7489	27.45 / 0.8254	32.03 / 0.9260
	ART-S [45]	ICLR23	11.87	55.6	32.86 / 0.9029	29.09 / 0.7942	27.91 / 0.7489	27.54 / 0.8261	32.13 / 0.9263
	HAT-S [22]	CVPR23	9.61	54.9	32.92 / 0.9047	29.15 / 0.7958	27.97 / 0.7505	<u>27.87</u> / <u>0.8346</u>	<u>32.35</u> / <u>0.9283</u>
	DAT-S [64]	ICCV23	11.21	50.8	33.00 / 0.9047	<u>29.20</u> / <u>0.7962</u>	27.97 / 0.7510	27.68 / 0.8300	32.33 / 0.9278
	SRFormer [23]	ICCV23	10.52	54.3	32.93 / 0.9041	29.08 / 0.7953	27.94 / 0.7502	27.68 / 0.8311	32.21 / 0.9271
	FDRNet [65]	TIP24	8.81	N/A	32.82 / 0.9339	29.11 / 0.7947	27.94 / 0.7494	27.63 / 0.8301	32.17 / 0.9264
	MambaIR [62]	ECCV24	20.57	82.2	33.03 / 0.9046	<u>29.20</u> / <u>0.7961</u>	27.98 / 0.7503	27.68 / 0.8287	33.32 / 0.9272
	MAT	Ours	9.74	49.2	<u>33.06</u> / <u>0.9054</u>	29.17 / 0.7960	<u>27.99</u> / <u>0.7514</u>	27.78 / 0.8328	32.31 / 0.9282
	MAT+	Ours	9.74	49.2	33.08 / 0.9056	29.24 / 0.7972	28.02 / 0.7520	27.89 / 0.8349	32.49 / 0.9294

improvements of approximately **0.8dB** and **0.9dB** on Urban100 and Manga109 datasets, respectively. When compared to Transformer-based models, MAT-light shows significant gains of **0.2dB~0.46dB** on the Manga109 dataset. Furthermore, our model outperforms the recent Mamba-based architecture, MambaIR-light, consistently across all evaluation metrics.

Visual Comparison. As shown in Fig. 9 and 12, we compare the visual results between MAT-light and other lightweight image SR models. MAT-light successfully recovers fine lines and texture details in the images, while others produce blurry artifacts and inaccurate details. These visual results demonstrate MAT-light's superior reconstruction capability through its effective feature extraction across different spatial ranges.

D. Classical Image Super-Resolution

To further demonstrate the scalability of MAT, we expand MAT to build a large model and compare it with a series of state-of-the-art classical SR methods: EDSR [10], RCAN [16], IGNN [31], NLSN [18], SwinIR [21], ART [45], HAT [22],

DAT [64], SRFormer [23], FDRNet [65] and MambaIR [62]. Consistent with prior works [21], [23], [45], self-ensemble strategy is introduced in testing to further improve the model's performance, denoted by the symbol "+".

Quantitative Comparison. Table VII shows the quantitative comparison of classical image SR models. MAT achieves superior performance across all five benchmark datasets and scale factors while requiring minimal parameters and computational complexity. Through its multi-range attention mechanism and feature modeling, MAT effectively captures hierarchical image features. The performance gains are further enhanced when applying the self-ensemble strategy, demonstrating MAT's effectiveness and scalability.

Visual Comparison. Fig. 13 presents the visual comparison between MAT and other classical image SR models. MAT accurately reconstructs the main image structures with fewer blur artifacts compared to other methods. This superior reconstruction quality stems from MAT's ability to capture features at multiple spatial ranges.

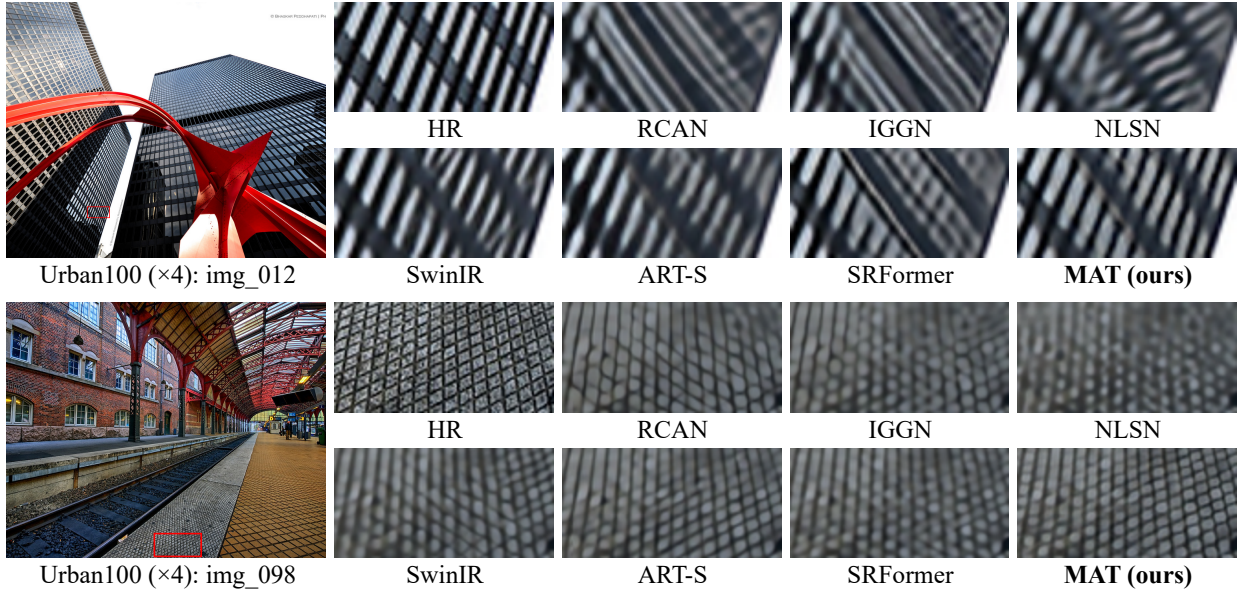


Fig. 13. Visual comparison on $\times 4$ classical image SR. The patches for comparison are marked with red boxes in the original images.

TABLE VIII

THE MODEL DEPTH AND PERFORMANCE COMPARISONS ON $\times 4$ SR. 'MULTI-ADDS', 'RUNNING TIME' AND 'MEMORY' IS CALCULATED UNDER THE SETTING OF UPSCALING ONE IMAGE TO 1280×720 RESOLUTION. THE BEST AND SECOND BEST RESULTS ARE MARKED IN RED AND BLUE COLORS, RESPECTIVELY.

Method	#Params. (K)	Multi-Adds (G)	#Depth Layers (Blocks)	#Time (ms)	#Mem. (G)	Set5		Set14		B100		Urban100		Manga109	
						PSNR / SSIM	PSNR / SSIM	PSNR / SSIM							
SwinIR-light	930	65.2	103 (24)	143.5	6.3	32.44 / 0.8980	28.83 / 0.7870	27.73 / 0.7418	26.47 / 0.7980	30.92 / 0.9151					
SRFormer-light	873	62.8	127 (24)	162.9	7.4	32.51 / 0.8988	28.82 / 0.7872	27.73 / 0.7422	26.67 / 0.8032	31.17 / 0.9165					
MAT-light	714	48.5	107 (20)	71.1	5.3	32.61 / 0.8998	28.92 / 0.7897	27.79 / 0.7444	26.83 / 0.8088	31.38 / 0.9192					
MAT-light-V2	956	66.4	147 (28)	105.5	7.6	32.68 / 0.9010	29.01 / 0.7915	27.84 / 0.7460	26.99 / 0.8129	31.51 / 0.9206					

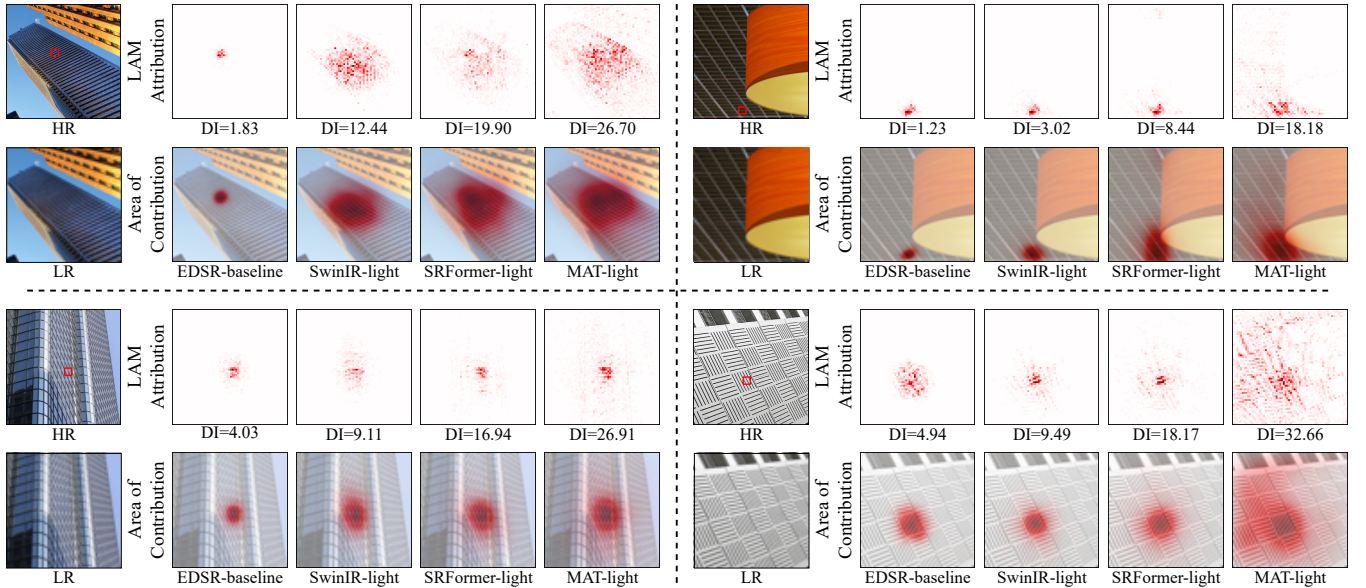


Fig. 14. Comparison of LAM results of EDSR-baseline [10], SwinIR-light [21], SRFormer-light [23], and the proposed MAT-light.

E. Model Depth Analyses

The depth of the model exerts a significant influence on computational efficiency. Table VIII presents a comparative analysis of model depth and performance. MAT achieves competitive performance and efficiency in its current depth configuration through the multi-range attention mechanism.

Notably, by increasing the number of RMAGs to 6 in MAT-light to align its capacity with comparable architectures, our MAT-light-V2 achieves greater performance gains while maintaining a shorter runtime. These results demonstrate the computational efficiency of our proposed MAT architecture.

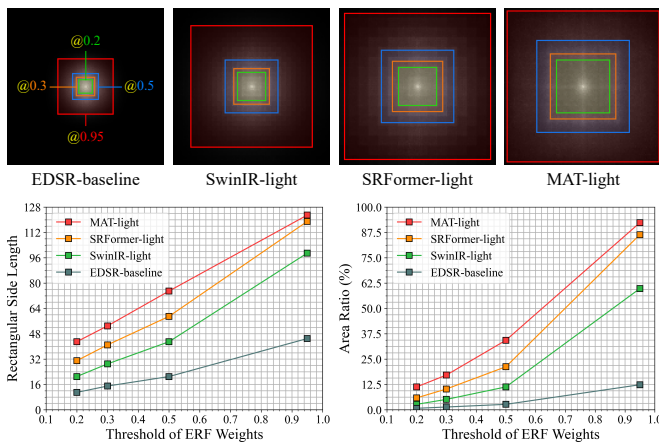


Fig. 15. The effective receptive field (ERF) [24] visualization and comparison for EDSR-baseline [10], SwinIR-light [21], SRFormer-light [23], and the proposed MAT-light. A larger ERF is indicated by a more extensively distributed bright area.

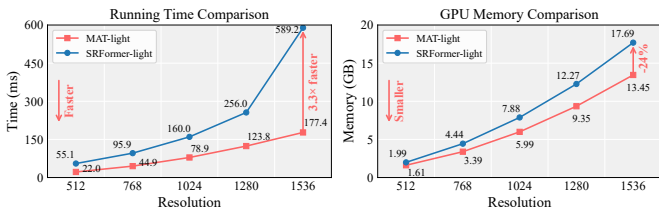


Fig. 16. Running time and memory comparisons on $\times 4$ SR.

F. Analyses of LAM and ERF

We use local attribution maps (LAM) [20] to visualize the spatial range of information used in target area reconstruction. As shown in Fig. 14, MAT-light effectively identifies and focuses on structurally similar regions across non-local spatial ranges while suppressing dissimilar features, whereas other methods are limited to local feature extraction. Quantitatively, MAT-light achieves significantly higher diffusion index (DI) values compared to other models. We also evaluate the effective receptive field (ERF) [24] to measure the actual receptive field. Fig. 15 shows the comparison of ERF rectangular side length and area ratio under different weight thresholds. MAT-light demonstrates a larger ERF, enabling broader information perception. These results validate the effectiveness of the multi-range representation learning.

G. Running Time and Memory Comparisons

We evaluate the computational efficiency of MAT-light with the representative Transformer-based model SRFormer-light [23] for $\times 4$ SR tasks. We measure average running time across 100 test images and peak GPU memory consumption during inference on an RTX 3090. As shown in Fig. 16, SRFormer-light requires longer running time and higher memory usage due to its large window sizes, which involve additional padding pixels and shift operations. In contrast, MAT-light demonstrates significant efficiency gains. For generating an HR image of 1536^2 resolution, MAT-light runs approximately $3.3\times$ faster than SRFormer-light while reducing GPU memory consumption by 24%.

V. CONCLUSION

In this paper, we present MAT, a highly effective model for image SR. MAT combines dilated operations with self-attention mechanisms to implement multi-range attention, enabling flexible attention scopes and enhanced perception of both regional and sparse global features. By integrating this with local feature extraction, MAT achieves effective multi-range representation learning. We also introduce the MSConvStar module, a streamlined enhancement to image token interconnections. Thorough experiments validate MAT's effectiveness and efficiency, with MAT achieving state-of-the-art performance in both lightweight and classical SR while requiring fewer parameters and lower computational costs.

REFERENCES

- [1] P. Weinzaepfel, H. Jégou, and P. Pérez, "Reconstructing an image from its local descriptors," in *CVPR*. IEEE, 2011, pp. 337–344. 1
- [2] X. Zhang, T. Li, and X. Zhao, "Boosting single image super-resolution via partial channel shifting," in *ICCV*, 2023, pp. 13 223–13 232. 1, 2
- [3] E. Shechtman and M. Irani, "Matching local self-similarities across images and videos," in *CVPR*, 2007, pp. 1–8. 1
- [4] D. Glasner, S. Bagon, and M. Irani, "Super-resolution from a single image," in *ICCV*, 2009, pp. 349–356. 1
- [5] Y. Hu, J. Li, Y. Huang, and X. Gao, "Image super-resolution with self-similarity prior guided network and sample-discriminating learning," *TCSVT*, vol. 32, no. 4, pp. 1966–1985, Apr. 2022. 1
- [6] J.-B. Huang, A. Singh, and N. Ahuja, "Single image super-resolution from transformed self-exemplars," in *CVPR*, 2015, pp. 5197–5206. 1, 5
- [7] C. Dong, C. C. Loy, K. He, and X. Tang, "Image super-resolution using deep convolutional networks," *IEEE TPAMI*, vol. 38, no. 2, pp. 295–307, 2015. 1, 2
- [8] J. Kim, J. K. Lee, and K. M. Lee, "Accurate image super-resolution using very deep convolutional networks," in *CVPR*, 2016, pp. 1646–1654. 1, 2
- [9] C. Ledig, L. Theis, F. Huszár, J. Caballero, A. Cunningham, A. Acosta, A. Aitken, A. Tejani, J. Totz, Z. Wang *et al.*, "Photo-realistic single image super-resolution using a generative adversarial network," in *CVPR*, 2017, pp. 4681–4690. 1
- [10] B. Lim, S. Son, H. Kim, S. Nah, and K. Mu Lee, "Enhanced deep residual networks for single image super-resolution," in *CVPR Workshops*, 2017, pp. 136–144. 1, 2, 5, 7, 8, 9, 10, 11
- [11] Y. Zhang, Y. Tian, Y. Kong, B. Zhong, and Y. Fu, "Residual dense network for image super-resolution," in *CVPR*, 2018, pp. 2472–2481. 2
- [12] H. Wu, Z. Zou, J. Gui, W.-J. Zeng, J. Ye, J. Zhang, H. Liu, and Z. Wei, "Multi-grained attention networks for single image super-resolution," *IEEE TCSVT*, vol. 31, no. 2, pp. 512–522, 2021. 2
- [13] Z. Hui, X. Gao, Y. Yang, and X. Wang, "Lightweight image super-resolution with information multi-distillation network," in *ACM MM*, 2019, pp. 2024–2032. 2, 3, 7, 8
- [14] Z. Li, Y. Liu, X. Chen, H. Cai, J. Gu, Y. Qiao, and C. Dong, "Blueprint separable residual network for efficient image super-resolution," in *CVPR Workshops*, 2022, pp. 833–843. 2
- [15] C. Xie, X. Zhang, L. Li, H. Meng, T. Zhang, T. Li, and X. Zhao, "Large kernel distillation network for efficient single image super-resolution," in *CVPR Workshops*, 2023, pp. 1283–1292. 2
- [16] Y. Zhang, K. Li, K. Li, L. Wang, B. Zhong, and Y. Fu, "Image super-resolution using very deep residual channel attention networks," in *ECCV*, 2018, pp. 286–301. 2, 3, 5, 9
- [17] J. Liu, W. Zhang, Y. Tang, J. Tang, and G. Wu, "Residual feature aggregation network for image super-resolution," in *CVPR*, 2020, pp. 2359–2368. 2
- [18] Y. Mei, Y. Fan, and Y. Zhou, "Image super-resolution with non-local sparse attention," in *CVPR*, 2021, pp. 3517–3526. 2, 4, 9
- [19] A. Vaswani, N. Shazeer, N. Parmar, J. Uszkoreit, L. Jones, A. N. Gomez, Ł. Kaiser, and I. Polosukhin, "Attention is all you need," *NeurIPS*, vol. 30, 2017. 2, 4, 5
- [20] J. Gu and C. Dong, "Interpreting super-resolution networks with local attribution maps," in *CVPR*, 2021, pp. 9199–9208. 2, 6, 7, 11
- [21] J. Liang, J. Cao, G. Sun, K. Zhang, L. Van Gool, and R. Timofte, "Swinir: Image restoration using swin transformer," in *ICCV Workshops*, 2021, pp. 1833–1844. 2, 3, 4, 5, 6, 7, 8, 9, 10, 11

- [22] X. Chen, X. Wang, J. Zhou, Y. Qiao, and C. Dong, "Activating more pixels in image super-resolution transformer," in *CVPR*, 2023, pp. 22 367–22 377. 2, 3, 9
- [23] Y. Zhou, Z. Li, C.-L. Guo, S. Bai, M.-M. Cheng, and Q. Hou, "Srformer: Permuted self-attention for single image super-resolution," in *ICCV*, 2023, pp. 12 780–12 791. 2, 3, 4, 5, 6, 7, 8, 9, 10, 11
- [24] X. Ding, X. Zhang, J. Han, and G. Ding, "Scaling up your kernels to 31x31: Revisiting large kernel design in cnns," in *CVPR*, 2022, pp. 11 963–11 975. 2, 11
- [25] Y. Li, Y. Fan, X. Xiang, D. Demandolx, R. Ranjan, R. Timofte, and L. Van Gool, "Efficient and explicit modelling of image hierarchies for image restoration," in *CVPR*, 2023, pp. 18 278–18 289. 2, 3
- [26] L.-C. Chen, G. Papandreou, F. Schroff, and H. Adam, "Rethinking atrous convolution for semantic image segmentation," *arXiv preprint arXiv:1706.05587*, 2017. 2
- [27] P. Wang, P. Chen, Y. Yuan, D. Liu, Z. Huang, X. Hou, and G. Cottrell, "Understanding convolution for semantic segmentation," in *WACV*, 2018, pp. 1451–1460. 2
- [28] X. Ma, X. Dai, Y. Bai, Y. Wang, and Y. Fu, "Rewrite the stars," in *CVPR*, Jun. 2024, pp. 5694–5703. 2, 5
- [29] E. Agustsson and R. Timofte, "Ntire 2017 challenge on single image super-resolution: Dataset and study," in *CVPR Workshops*, 2017, pp. 126–135. 2, 5
- [30] S. Ioffe and C. Szegedy, "Batch normalization: Accelerating deep network training by reducing internal covariate shift," in *ICML*, vol. 37, Jul. 2015, pp. 448–456. 2
- [31] S. Zhou, J. Zhang, W. Zuo, and C. C. Loy, "Cross-scale internal graph neural network for image super-resolution," *NeurIPS*, vol. 33, pp. 3499–3509, 2020. 2, 9
- [32] H. Wu, J. Gui, J. Zhang, J. T. Kwok, and Z. Wei, "Feedback pyramid attention networks for single image super-resolution," *IEEE TCSVT*, vol. 33, no. 9, pp. 4881–4892, Sep. 2023. 2
- [33] X. Wang, R. Girshick, A. Gupta, and K. He, "Non-local neural networks," in *CVPR*, 2018, pp. 7794–7803. 2
- [34] A. Dosovitskiy, L. Beyer, A. Kolesnikov, D. Weissenborn, X. Zhai, T. Unterthiner, M. Dehghani, M. Minderer, G. Heigold, S. Gelly *et al.*, "An image is worth 16x16 words: Transformers for image recognition at scale," in *ICLR*, 2021. 3, 4
- [35] Z. Liu, Y. Lin, Y. Cao, H. Hu, Y. Wei, Z. Zhang, S. Lin, and B. Guo, "Swin transformer: Hierarchical vision transformer using shifted windows," in *ICCV*, 2021, pp. 10 012–10 022. 3, 4
- [36] E. Xie, W. Wang, Z. Yu, A. Anandkumar, J. M. Alvarez, and P. Luo, "Segformer: Simple and efficient design for semantic segmentation with transformers," *NeurIPS*, vol. 34, pp. 12 077–12 090, 2021. 3
- [37] N. Carion, F. Massa, G. Synnaeve, N. Usunier, A. Kirillov, and S. Zagoruyko, "End-to-end object detection with transformers," in *ECCV*, 2020, pp. 213–229. 3
- [38] S. W. Zamir, A. Arora, S. Khan, M. Hayat, F. S. Khan, and M.-H. Yang, "Restormer: Efficient transformer for high-resolution image restoration," in *CVPR*, 2022, pp. 5728–5739. 3, 5
- [39] W. Guan, X. Song, K. Wang, H. Wen, H. Ni, Y. Wang, and X. Chang, "Egocentric early action prediction via multimodal transformer-based dual action prediction," *IEEE TCSVT*, vol. 33, no. 9, pp. 4472–4483, 2023. 3
- [40] Y. Yu, R. Ni, Y. Zhao, S. Yang, F. Xia, N. Jiang, and G. Zhao, "Msvt: Multiple spatiotemporal views transformer for deepfake video detection," *IEEE TCSVT*, vol. 33, no. 9, pp. 4462–4471, Sep. 2023. 3
- [41] M. Li, B. Ma, and Y. Zhang, "Lightweight image super-resolution with pyramid clustering transformer," *IEEE TCSVT*, 2023. 3
- [42] J. Wang, B. Wang, X. Wang, Y. Zhao, and T. Long, "Hybrid attention-based u-shaped network for remote sensing image super-resolution," *IEEE TGRS*, vol. 61, pp. 1–15, 2023. 3
- [43] Y. Lu, L. Min, B. Wang, L. Zheng, X. Wang, Y. Zhao, L. Yang, and T. Long, "Cross-spatial pixel integration and cross-stage feature fusion-based transformer network for remote sensing image super-resolution," *IEEE TGRS*, vol. 61, pp. 1–16, 2023. 3
- [44] H. Wang, X. Chen, B. Ni, Y. Liu, and J. Liu, "Omni aggregation networks for lightweight image super-resolution," in *CVPR*, 2023, pp. 22 378–22 387. 3, 7, 8
- [45] J. Zhang, Y. Zhang, J. Gu, Y. Zhang, L. Kong, and X. Yuan, "Accurate image restoration with attention retractable transformer," in *ICLR*, 2023. 3, 6, 9
- [46] Z. Li, J. Li, L. Ren, and Z. Chen, "Transformer-based dual-branch multiscale fusion network for pan-sharpening remote sensing images," *IEEE JSTARS*, vol. 17, pp. 614–632, 2023. 3
- [47] X. Pan, T. Ye, Z. Xia, S. Song, and G. Huang, "Slide-transformer: Hierarchical vision transformer with local self-attention," in *CVPR*, 2023, pp. 2082–2091. 3
- [48] J. Jiao, Y.-M. Tang, K.-Y. Lin, Y. Gao, A. J. Ma, Y. Wang, and W.-S. Zheng, "Dilateformer: Multi-scale dilated transformer for visual recognition," *TMM*, vol. 25, pp. 8906–8919, 2023. 3
- [49] W. Shi, J. Caballero, F. Huszár, J. Totz, A. P. Aitken, R. Bishop, D. Rueckert, and Z. Wang, "Real-time single image and video super-resolution using an efficient sub-pixel convolutional neural network," in *CVPR*, 2016, pp. 1874–1883. 3
- [50] B. Xia, Y. Hang, Y. Tian, W. Yang, Q. Liao, and J. Zhou, "Efficient non-local contrastive attention for image super-resolution," in *AAAI*, vol. 36, 2022, pp. 2759–2767. 4
- [51] P. Ramachandran, N. Parmar, A. Vaswani, I. Bello, A. Levskaya, and J. Shlens, "Stand-alone self-attention in vision models," *NeurIPS*, vol. 32, 2019. 4
- [52] A. Hassani, S. Walton, J. Li, S. Li, and H. Shi, "Neighborhood attention transformer," in *CVPR*, 2023, pp. 6185–6194. 4
- [53] A. Vaswani, P. Ramachandran, A. Srinivas, N. Parmar, B. Hechtman, and J. Shlens, "Scaling local self-attention for parameter efficient visual backbones," in *CVPR*, 2021, pp. 12 894–12 904. 4
- [54] A. Li, L. Zhang, Y. Liu, and C. Zhu, "Exploring frequency-inspired optimization in transformer for efficient single image super-resolution," *IEEE TPAMI*, pp. 1–18, 2025. 5, 7, 8
- [55] M. Bevilacqua, A. Roumy, C. Guillemot, and M. L. Alberi-Morel, "Low-complexity single-image super-resolution based on nonnegative neighbor embedding," in *BMVC*, 2012. 5
- [56] R. Zeyde, M. Elad, and M. Protter, "On single image scale-up using sparse-representations," in *Curves and Surfaces*, 2012, pp. 711–730. 5
- [57] D. Martin, C. Fowlkes, D. Tal, and J. Malik, "A database of human segmented natural images and its application to evaluating segmentation algorithms and measuring ecological statistics," in *ICCV*, vol. 2, 2001, pp. 416–423. 5
- [58] Y. Matsui, K. Ito, Y. Aramaki, A. Fujimoto, T. Ogawa, T. Yamasaki, and K. Aizawa, "Sketch-based manga retrieval using manga109 dataset," *Multimed Tools Appl*, vol. 76, pp. 21 811–21 838, 2017. 5
- [59] D. P. Kingma and J. Ba, "Adam: A method for stochastic optimization," *arXiv preprint arXiv:1412.6980*, 2014. 5
- [60] X. Luo, Y. Xie, Y. Zhang, Y. Qu, C. Li, and Y. Fu, "Latticenet: Towards lightweight image super-resolution with lattice block," in *ECCV*, 2020, pp. 272–289. 7, 8
- [61] H. Choi, J. Lee, and J. Yang, "N-gram in swin transformers for efficient lightweight image super-resolution," in *CVPR*, 2023, pp. 2071–2081. 7, 8
- [62] H. Guo, J. Li, T. Dai, Z. Ouyang, X. Ren, and S.-T. Xia, "Mambair: A simple baseline for image restoration with state-space model," in *ECCV*, 2024. 7, 8, 9
- [63] F. Li, R. Cong, J. Wu, H. Bai, M. Wang, and Y. Zhao, "Srconvnet: A transformer-style convnet for lightweight image super-resolution," *IJCV*, vol. 133, no. 1, pp. 173–189, 2025. 7, 8
- [64] Z. Chen, Y. Zhang, J. Gu, L. Kong, X. Yang, and F. Yu, "Dual aggregation transformer for image super-resolution," in *ICCV*, 2023, pp. 12 312–12 321. 9
- [65] Y. Zuo, W. Yao, Y. Hu, Y. Fang, W. Liu, and Y. Peng, "Image super-resolution via efficient transformer embedding frequency decomposition with restart," *IEEE TIP*, vol. 33, pp. 4670–4685, 2024. 9